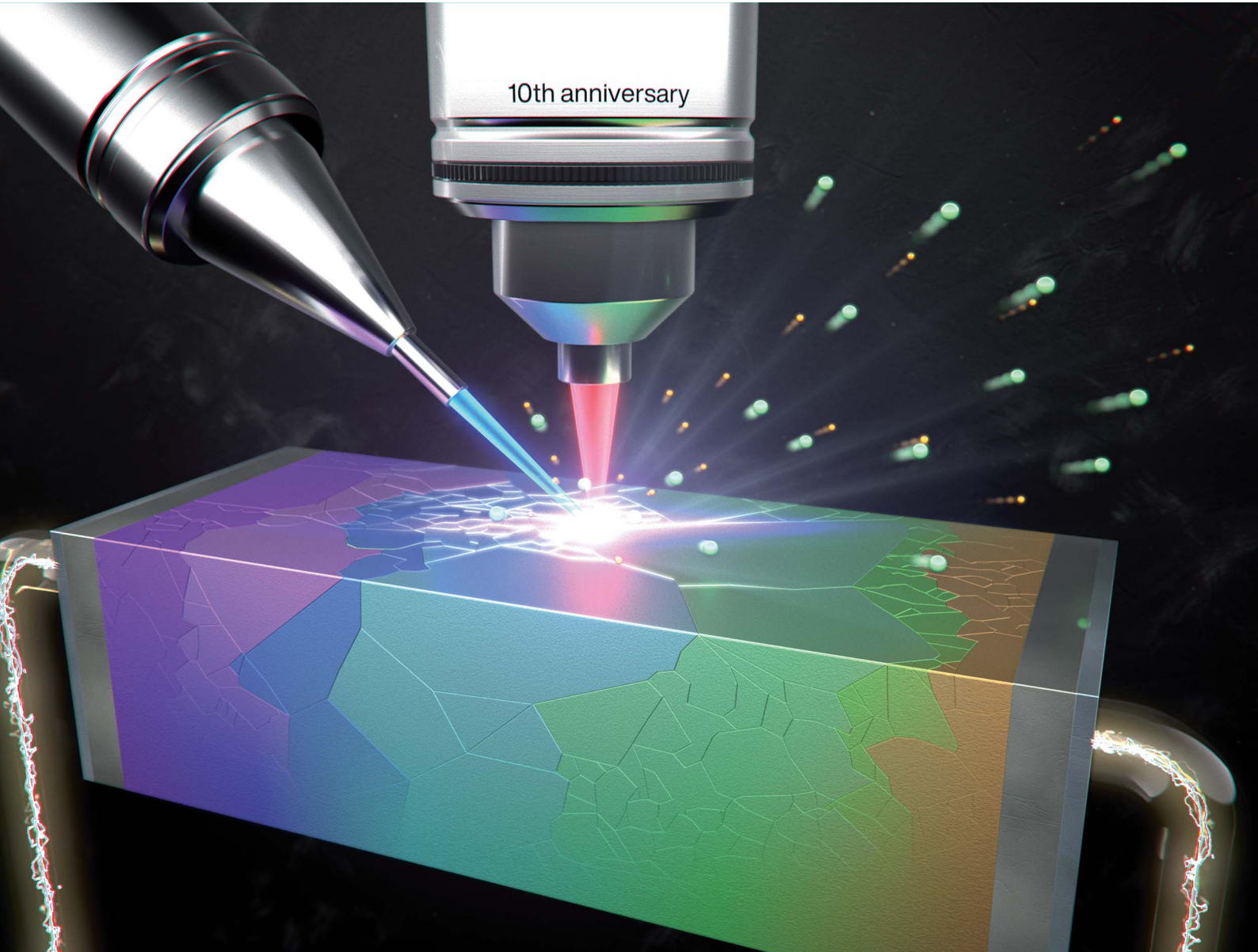


Journal of Materials Chemistry A

Materials for energy and sustainability

rsc.li/materials-a

10th anniversary



ISSN 2050-7488

PAPER

Naoaki Kuwata *et al.*
Visualization and evaluation of lithium diffusion at grain
boundaries in $\text{Li}_{0.29}\text{La}_{0.57}\text{TiO}_3$ solid electrolytes using
secondary ion mass spectrometry



Cite this: *J. Mater. Chem. A*, 2024, **12**, 731

Visualization and evaluation of lithium diffusion at grain boundaries in $\text{Li}_{0.29}\text{La}_{0.57}\text{TiO}_3$ solid electrolytes using secondary ion mass spectrometry†

Gen Hasegawa, Naoaki Kuwata, * Tsuyoshi Ohnishi and Kazunori Takada

Understanding Li diffusion at interfaces in solid-state Li batteries is essential to improving their performance (e.g., rate capabilities and energy densities). However, the visualization of Li diffusion at grain boundaries has been impossible due to the lack of experimental techniques. In this study, we visualize Li-ion diffusion at grain boundaries *via* secondary ion mass spectrometry at low temperatures (≈ -110 °C) using an isotope exchange technique for perovskite-type $\text{Li}_{0.29}\text{La}_{0.57}\text{TiO}_3$ as a model solid electrolyte. The grain boundary diffusion coefficient obtained in this study is $1.4 \times 10^{-13} \text{ cm}^2 \text{ s}^{-1}$ at 25 °C, which is much smaller than the bulk diffusion coefficient of $2.6 \times 10^{-8} \text{ cm}^2 \text{ s}^{-1}$. The long-range effective diffusion coefficients can be explained well by a 1D model based on a series of bulk and grain boundaries. The Haven ratio of grain boundary diffusion suggests that correlation between the Li^+ ions is crucial for grain boundary diffusion.

Received 21st August 2023
Accepted 4th November 2023
DOI: 10.1039/d3ta05012b
rsc.li/materials-a

Introduction

Solid-state Li batteries are expected to serve as next-generation energy storage systems due to their safety, reliability, and high energy densities.¹ However, a significant challenge lies in the ion dynamics at the grain boundaries and the interfaces between the active materials and electrolytes.²⁻⁴ High resistance at the cathode/electrolyte interface leads to poor power density of solid-state batteries with sulfide-based solid electrolytes, and it has been successfully lowered by interposition of thin films at the interface.⁵ Now, sulfide-based solid-state batteries show practical performance, and they are under development aiming at application to electric vehicles.⁶ One of the disadvantages of sulfide-based solid-state batteries is the instability of the solid electrolytes. Sulfide electrolytes are easily decomposed in a humid atmosphere and release harmful hydrogen sulfide upon the decomposition.⁷ This concern has brought about a lot of efforts to replace the sulfide electrolytes with oxides. However, oxide-based solid electrolyte batteries also show high interfacial resistance at grain boundaries.^{2,8} Therefore, although oxide-based solid electrolytes have achieved ionic conductivities of the order of $10^{-3} \text{ S cm}^{-1}$, the internal resistance of oxide-based solid-state batteries is still high, resulting in poor battery performance. In order to achieve practical battery performance, it is necessary to elucidate the origin of

grain boundary resistance and find a way to reduce it, for which techniques to evaluate the interfacial ion dynamics are essential.

The analysis of ion dynamics in solid-state Li battery materials has focused mainly on the average ionic conductivity obtained using impedance spectroscopy (IS), the bulk diffusion coefficient obtained using pulsed-field gradient nuclear magnetic resonance (PFG-NMR) spectroscopy, and relaxation time measurements using NMR spectroscopy (Fig. 1). The interfaces of solid-state Li batteries are observed using scanning transmission electron and scanning electron microscopy (SEM). The chemical diffusion of Li^+ ions at the grain boundaries of $\text{LiNi}_{0.8}\text{Co}_{0.15}\text{Al}_{0.05}\text{O}_2$ cathode materials has been analyzed using electron energy-loss spectroscopy.⁹ Additionally, Kimura *et al.* used computed tomography combined with X-ray absorption near-edge structure spectroscopy to visualize the distribution of the chemical diffusion in LiCoO_2 particles.¹⁰ However, these methods observe chemical diffusion with Li concentration change and cannot measure ion dynamics in solid electrolytes or at the interface between the electrolyte and active material without Li concentration change. Electrochemical strain microscopy is a technique for visualizing the bulk and grain boundary conductivities of solid electrolytes, although several assumptions are required.¹¹

Tracer diffusion analysis based on secondary ion mass spectrometry (SIMS) is an effective tool for quantitatively analyzing ion diffusion in solid electrolytes and active materials.¹²⁻²³ Additionally, SIMS enables a wide range of ionic diffusion measurements from the nanometer to the millimeter scale, but it is limited in analyzing fast ionic conductors

Research Center for Energy and Environmental Materials (GREEN), National Institute for Materials Science (NIMS), 1-1 Namiki, Tsukuba, Ibaraki 305-0044, Japan. E-mail: KUAWATA.Naoaki@nims.go.jp

† Electronic supplementary information (ESI) available. See DOI: <https://doi.org/10.1039/d3ta05012b>



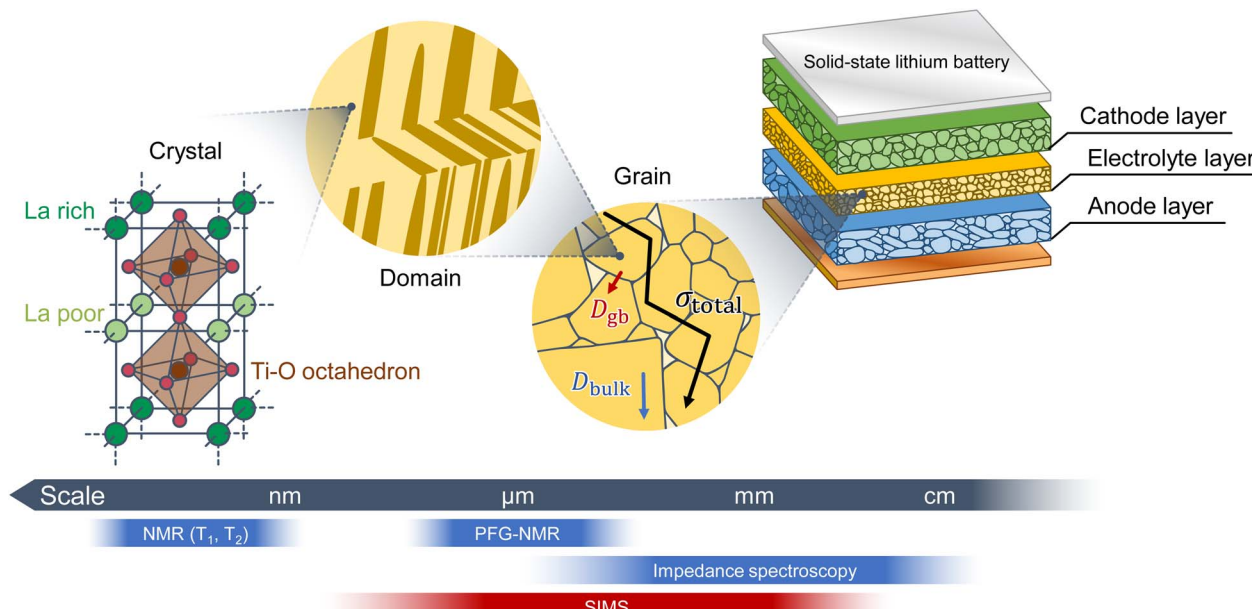


Fig. 1 Multiscale ion dynamics in solid-state batteries and their measurement techniques. The average ionic conductivity can be measured by IS. PFG-NMR spectroscopy measures ion diffusion on the micrometer scale, and secondary ion mass spectrometry (SIMS) can determine the ion diffusion coefficients over a wide spatial range from millimeters to tens of nanometers.

because the primary ion beam disrupts the ion distributions in solid electrolytes.²⁴ Téllez *et al.* suggested that the Li distribution is maintained *via* analysis at low temperatures, even in fast ionic conductors, such as perovskite-type solid electrolytes.²⁴ SIMS at low temperatures is known as cryo-SIMS, because it suppresses sample damage.^{25,26}

In this study, perovskite-type solid electrolytes are analyzed using SIMS. We have established high-resolution SIMS techniques for imaging the isotope distributions in polycrystalline solid electrolytes and succeeded in quantitatively evaluating the tracer diffusion coefficients of bulk and grain boundaries. Furthermore, we quantify the grain boundary diffusion coefficient, which indicated that the grain boundaries are the rate-limiting factors in the total conductivity. We use $\text{Li}_{0.29}\text{La}_{0.57}\text{TiO}_3$ (LLTO), which is a fast Li-ion conductor with an ionic conductivity of $10^{-3} \text{ S cm}^{-1}$ at 27°C ,²⁷⁻³⁰ as the model material.

Cambridge Isotope Laboratories, Tewksbury, MA, USA) and HNO_3 (65 wt%, FUJIFILM Wako Pure Chemical, Osaka, Japan) in a 1 : 2 molar ratio. Fig. 2 shows the process of ${}^6\text{Li}$ exchange and SIMS measurement. The edge of the LLTO was immersed in the aqueous ${}^6\text{LiNO}_3$ solution for ${}^6\text{Li}$ isotope exchange for 59–110 h, and the sample was then cooled to -110°C in a SIMS system and the surface ${}^6\text{Li}$ isotope ratio was observed *via* SIMS. After SIMS, diffusion was further enhanced by annealing at 22–400 °C. The sample was again cooled to -110°C and analyzed using SIMS. This procedure enabled the measurement of the temperature dependence of the diffusion coefficient.

To prevent the potential effects of thermal etching on grain boundaries, the sample preparations and measurements were proceeded in the following sequence: (i) polishing, (ii) isotope exchange, (iii) SIMS, (iv) further diffusion (22–400 °C), (v) SIMS, (vi) thermal etching (1100 °C), and (vii) optical microscopy.

Experimental

Sample preparation

LLTO polycrystals sintered at 1450°C were purchased from Toho Titanium (Yokohama, Japan). The samples were cut into $5 \times 10 \times 0.5 \text{ mm}^3$ pieces using a pen-type diamond glass cutter and ground using 800, 1200, and 2500 grit sandpaper, followed by 2 and $0.5 \mu\text{m}$ diamond lapping films. The specimens were polished using Baikalox 0.1CR agglomerate-free alumina and colloidal silica in deionized water. The polished sample surfaces were etched at 1100°C for 1 h in air to visualize the grain boundaries. Surface observations were performed using laser microscopy (VK-9710, Keyence, Osaka, Japan). A ${}^6\text{LiNO}_3$ solution (5 mol L^{-1}) was used in the isotope exchange studies. ${}^6\text{LiNO}_3$ was prepared by mixing ${}^6\text{Li}_2\text{CO}_3$ (95% ${}^6\text{Li}$, 5% ${}^7\text{Li}$,

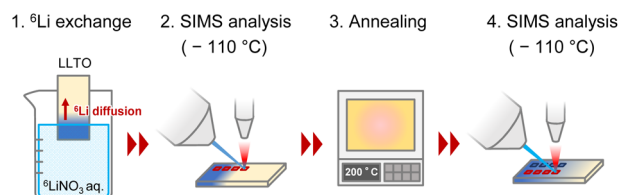


Fig. 2 Schematic diagram of the ${}^6\text{Li}$ isotope exchange study using LLTO. The edge of the LLTO is immersed in the aqueous ${}^6\text{LiNO}_3$ solution for exchange. The sample is immediately cooled to -110°C and SIMS is performed to observe the ${}^6\text{Li}$ isotope ratio. The sample is then annealed at 22–400 °C for further diffusion. The sample is again cooled to -110°C , and the ${}^6\text{Li}$ isotope ratio is measured. Repeating this procedure enables the determination of the temperature dependence of the diffusion coefficient.



SIMS measurement

Time-of-flight SIMS (TOF.SIMS 5, IONTOF, Münster, Germany) was used to measure the ${}^6\text{Li}$ isotope distribution. During SIMS, the samples were cooled to $-110\text{ }^\circ\text{C}$ with liquid N_2 to quench the ${}^6\text{Li}$ diffusion. The primary ion source was a single charge of Bi^+ with an acceleration voltage of 30 kV. An electron flood gun was used for charge compensation. The surface impurities were removed using an Ar gas cluster ion beam with a raster size of $700 \times 700 \mu\text{m}^2$ and an acceleration voltage of 10 kV. The raster size of the primary ion beam used in mapping measurements was $500 \times 200 \mu\text{m}^2$. The pixel resolution in SIMS imaging was 512×206 , and the spatial resolution was $1 \times 1 \mu\text{m}^2$. The primary ion current was 0.5 pA and the signal was integrated for 5 h to obtain one image. Line measurements were performed using a C_s sputter gun (acceleration voltage of 2 kV) with a depth analysis of approximately 500 nm to confirm uniformity in the depth direction. The respective raster sizes of the sputter and primary ion guns were set to 100×100 and $50 \times 50 \mu\text{m}^2$.

Results and discussion

Visualization of the isotope distributions in solid electrolytes

Fig. 3a illustrates the results of ${}^6\text{Li}$ isotope imaging using cryo-SIMS. LLTO was prepared *via* isotope exchange at $22\text{ }^\circ\text{C}$ for 59 h

and introduced into the SIMS system immediately after ${}^6\text{Li}$ exchange. During cryo-SIMS, the temperature was maintained at $-110\text{ }^\circ\text{C}$ to quench the Li diffusion. The relative ${}^6\text{Li}$ fraction C changes from the bottom to the top of the LLTO owing to the diffusion of the ${}^6\text{Li}$ isotope. $C (= {}^6\text{Li}/({}^6\text{Li} + {}^7\text{Li}))$ is obtained based on SIMS as follows:

$$C = \frac{I_{^6\text{Li}}}{I_{^6\text{Li}} + I_{^7\text{Li}}}, \quad (1)$$

where $I_{^6\text{Li}}$ and $I_{^7\text{Li}}$ are the intensities of the peaks for ${}^6\text{Li}$ and ${}^7\text{Li}$, respectively. The SIMS image in Fig. 3a clearly reveals that C changes rapidly at the grain boundaries *via* comparison with the laser microscope image taken from the same position in Fig. 3c, and thus, Li diffusion in the LLTO polycrystals is rate-limiting at the grain boundaries. This grain boundary resistance is the main factor increasing the total resistance of the polycrystalline solid electrolytes. Elucidating the origin of the grain boundary resistance (*i.e.*, grain boundary diffusivity) is one of the most important issues in the realization of solid-state batteries. Atomic diffusion at the grain boundaries is usually believed to be fast,³¹ and ionic conductivity increases at the grain boundaries in ionic conductors such as ZrO_2 .³² However, in solid electrolytes with fast ionic conduction pathways in their crystal structures, such as LLTO, diffusion at the grain

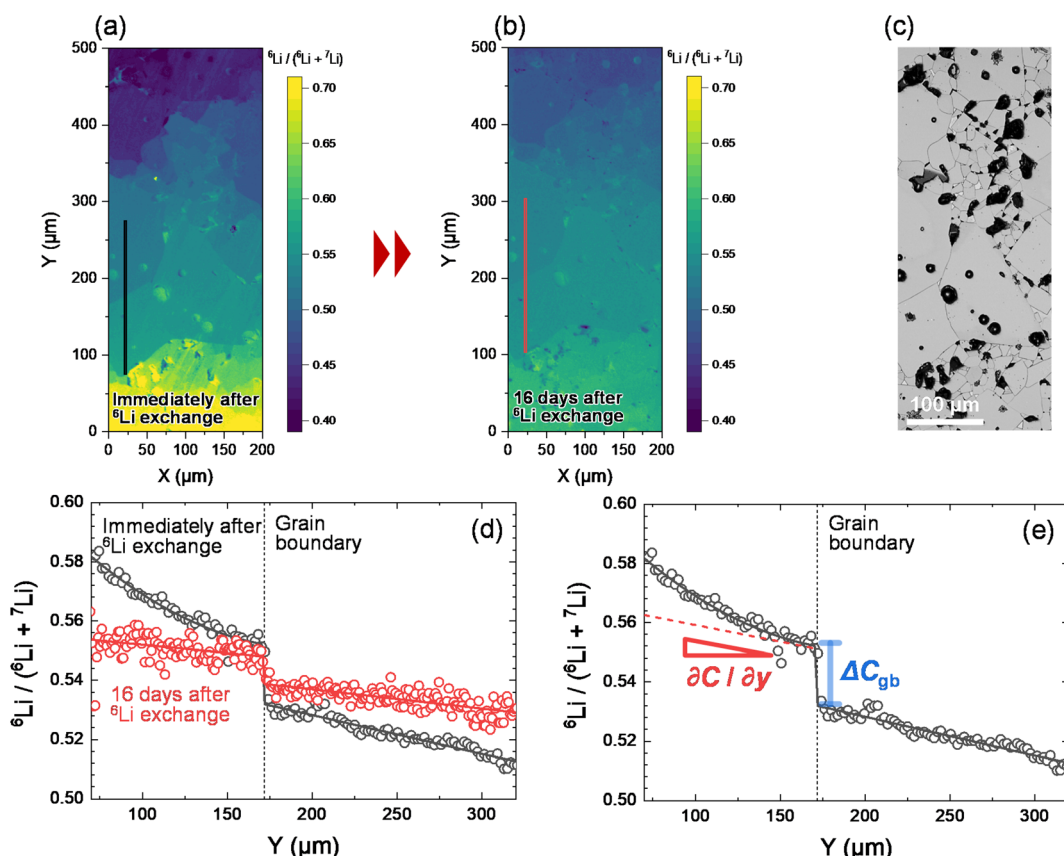


Fig. 3 (a) Imaging of the relative ${}^6\text{Li}$ fraction of LLTO immediately after ${}^6\text{Li}$ isotope exchange for 59 h and (b) after 16 d of storage in an Ar atmosphere at $22\text{ }^\circ\text{C}$. (c) Laser microscope image of LLTO in the same position as that used in SIMS. Thermal etching for grain boundary observation was performed after SIMS imaging. (d) ${}^6\text{Li}$ isotopic profiles of the black and red lines shown in the SIMS images. The black and red open circles respectively represent the profiles of the sample after 59 h and 16 d of isotope exchange. (e) Gradient of the ${}^6\text{Li}$ fraction $\partial C/\partial y$ and concentration difference ΔC_{gb} at the grain boundary.



boundaries is slower than that in the bulk materials. Fig. 3b shows the SIMS images of C in LLTO after diffusion at 22 °C for an additional 16 d. The ${}^6\text{Li}$ distribution becomes homogeneous *via* diffusion, but the ${}^6\text{Li}$ concentration still changes stepwise at the grain boundaries.

Fig. 3d compares the profiles of the C values along the black and red lines shown in the SIMS images, which indicates that C changes abruptly at the grain boundary. The continuity of the diffusion flux across the interface between the bulk and grain boundaries is expressed as

$$-D_{\text{bulk}}^* \frac{\partial C}{\partial y} \Big|_{\text{bulk}} = -D_{\text{gb}}^* \frac{\partial C}{\partial y} \Big|_{\text{gb}}, \quad (2)$$

where D_{bulk}^* and D_{gb}^* are the respective bulk and grain boundary diffusion coefficients, $\partial C/\partial y|_{\text{bulk}}$ is the ${}^6\text{Li}$ concentration gradient in the bulk nearby the boundary, and $\partial C/\partial y|_{\text{gb}}$ is the ${}^6\text{Li}$ concentration gradient at the grain boundary. If the grain boundary thickness δ is sufficiently thin, eqn (2) can be written as

$$-D_{\text{bulk}}^* \frac{\partial C}{\partial y} \Big|_{\text{bulk}} = -D_{\text{gb}}^* \frac{\Delta C_{\text{gb}}}{\delta}, \quad (3)$$

where ΔC_{gb} is the difference in the ${}^6\text{Li}$ concentration at the grain boundary (Fig. 3e). When D_{gb}^* is much lower than D_{bulk}^* , $\Delta C_{\text{gb}}/\delta$ must be larger than $\partial C/\partial y|_{\text{bulk}}$ to satisfy eqn (3). Therefore, when the diffusion is rate-limiting at the grain boundaries, C varies stepwise at the grain boundaries. Based on Fig. 3e, the derivative coefficient $\partial C/\partial y|_{\text{bulk}}$ is determined to be 1.1 cm^{-1} using a quadratic function, and ΔC_{gb} is 0.02. We assume that D_{bulk}^* is consistent with the diffusion coefficient $D_{\text{NMR,bulk}}$ determined *via* PFG-NMR spectroscopy,³³ with $D_{\text{NMR,bulk}}$ representing the average diffusion coefficient of randomly oriented LLTO crystals with 2D diffusion pathways. LLTO is known to have a 90° domain boundary microstructure,^{34,35} which is a 90° rotation of the alignment of La-rich and La-poor layers in the perovskite structure. This domain boundary may affect the diffusion behavior because LLTO has a two-dimensional diffusion pathway. The LLTO sample used in this study also contains 90° domains with a size of several hundreds of nanometers.³³ Despite the presence of such 90° domains, the SIMS image shown in Fig. 3a reveals uniform isotope concentrations within the grains and therefore uniform diffusion coefficients. This the bulk diffusion coefficient will be the value averaged through multiple domain boundaries. If a $D_{\text{NMR,bulk}}$ of $2.6 \times 10^{-8} \text{ cm}^2 \text{ s}^{-1}$ at 22 °C³³ is used, then $D_{\text{gb}}^*/\delta = 1.5 \times 10^{-6} \text{ cm}^2 \text{ s}^{-1}$. Assuming that the typical thickness $\delta = 0.5 \text{ nm}$,^{36,37} then $D_{\text{gb}}^* = 7.6 \times 10^{-14} \text{ cm}^2 \text{ s}^{-1}$, and the calculated D_{gb}^* is five orders of magnitude lower than $D_{\text{NMR,bulk}}$. Similarly, the SIMS profile after 16 d, as indicated by the red line shown in Fig. 3d, is analyzed, and $\partial C/\partial y|_{\text{bulk}}$ and ΔC_{gb} are 0.65 cm^{-1} and 0.009 , respectively. $D_{\text{gb}}^* = 9.2 \times 10^{-14} \text{ cm}^2 \text{ s}^{-1}$, which is consistent with the D_{gb}^* determined immediately after ${}^6\text{Li}$ exchange. Similar line analyses are performed at other grain boundaries. The results are shown in the ESI (Fig. S3 and Table S2†). The D_{gb}^* values for each grain boundary are in the range of 2.6×10^{-14} to $1.5 \times 10^{-13} \text{ cm}^2 \text{ s}^{-1}$. The average value is $6.8 \times 10^{-14} \text{ cm}^2 \text{ s}^{-1}$, which agrees with the D_{gb}^* value obtained from Fig. 3e. The above analysis reveals that D_{gb}^* values are low at most grain boundaries in LLTO.

Measurements of the long-range (effective) diffusion coefficients

The long-range diffusion coefficients are then measured using SIMS line analysis. Long-range diffusion in polycrystals comprising bulk and grain boundaries exhibits a single effective diffusion coefficient (D_{gb}^*) on the macroscopic scale.³⁸⁻⁴⁰ Fig. 4a shows the time evolution of the C of LLTO, as measured *via* SIMS line analysis. The black circles shown in Fig. 4a represent the ${}^6\text{Li}$ profile after 110 h of isotope exchange in contact with a ${}^6\text{LiNO}_3$ solution. C is constant in the region immersed in the solution (-1 to 0 mm , as shown in Fig. 4a), whereas above the liquid level (0 – 6 mm , as shown in Fig. 4a), a ${}^6\text{Li}$ concentration distribution is observed due to diffusion. When the origin of position x is the liquid surface, the ${}^6\text{Li}$ concentration $C(x, t)$ at $x = 0$ is regarded as constant, regardless of time t . The solution of the 1D diffusion equation is then expressed as^{41,42}

$$\frac{C(x, t) - C_0}{C_s - C_0} = \text{erfc} \left[\frac{x}{2\sqrt{D_{\text{eff}}^* t}} \right], \quad (4)$$

where C_s is the ${}^6\text{Li}$ fraction in the aqueous solution, C_0 is the initial ${}^6\text{Li}$ fraction in the LLTO polycrystal, and D_{eff}^* is the

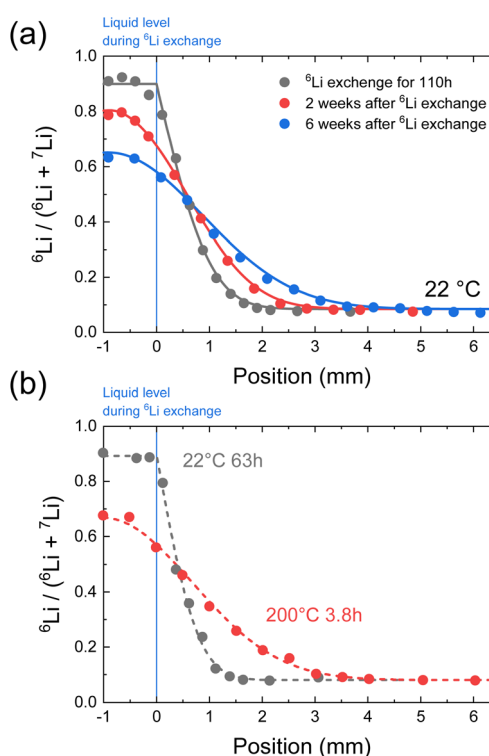


Fig. 4 (a) Time evolution of the relative ${}^6\text{Li}$ fraction of LLTO at 22 °C. The black circles represent the SIMS profile immediately after 110 h of ${}^6\text{Li}$ isotope exchange, and the red and blue circles represent the respective SIMS profiles after 2 and 6 weeks of storage in an Ar atmosphere. (b) Variation in the relative ${}^6\text{Li}$ fraction of LLTO after annealing at 200 °C. The black circles represent the SIMS profile immediately after ${}^6\text{Li}$ isotope exchange for 63 h, and the red circles represent the profile after annealing at 200 °C.

effective tracer diffusion coefficient. By fitting eqn (4) to the experimental data, as indicated by the solid black line shown in Fig. 4a, D_{eff}^* is determined to be $8.0 \times 10^{-9} \text{ cm}^2 \text{ s}^{-1}$. The red and blue circles shown in Fig. 4a indicate the ${}^6\text{Li}$ profiles of LLTO after storage in an Ar atmosphere for 2 and 6 weeks at 22°C , respectively. During storage, the sample did not come into contact with the ${}^6\text{LiNO}_3$ solution, and the total amount of ${}^6\text{Li}$ should be maintained. D_{eff}^* is obtained based on the time evolution of the ${}^6\text{Li}$ profile using a 1D numerical simulation of the diffusion equation. The initial conditions are indicated by the solid black line shown in Fig. 4a. The simulated results after storage for 2 and 6 weeks are shown as the red and blue solid lines, respectively, with a D_{eff}^* of $3.0 \times 10^{-9} \text{ cm}^2 \text{ s}^{-1}$ at 22°C . The D_{eff}^* determined immediately after ${}^6\text{Li}$ exchange is slightly larger than the D_{eff}^* of the stored sample. The D_{eff}^* immediately after ion exchange is likely overestimated due to the rise in the level of the upper surface of the liquid caused by the meniscus and the slight fluctuation in the liquid level. The D_{eff}^* determined using the time evolution of the ${}^6\text{Li}$ distribution is thus more accurate. Fig. 4b shows the effect of annealing at 200°C for 3.8 h after ${}^6\text{Li}$ exchange. The numerical simulations show that $D_{\text{eff}}^* = 6.6 \times 10^{-6} \text{ cm}^2 \text{ s}^{-1}$ at 200°C and the other D_{eff}^* values at different temperatures from 22 to 400°C were determined in a similar manner and used in the following discussion.

Relationship between D_{bulk}^* , D_{gb}^* , and D_{eff}^*

We analyze the relationship between D_{gb}^* , D_{bulk}^* , and D_{eff}^* based on a simple model. The Fisher model,⁴³ which is a well-known model of grain boundary diffusion, is suitable when grain boundary diffusion is faster than bulk diffusion, *e.g.*, in metals. However, in LLTO, $D_{\text{bulk}} \gg D_{\text{gb}}$, and the Fisher model is inappropriate. The brick layer³⁹ and Maxwell–Garnett models,³⁸ as shown in Fig. 5a, are generally used in modeling ion diffusion in polycrystalline materials. These models include two types of diffusion pathways: along and across grain boundaries. In LLTO, $D_{\text{bulk}} \gg D_{\text{gb}}$, and thus, diffusion along the grain boundaries is ignored. Therefore, the series model of the bulk and grain boundaries provides a good approximation. If the diffusion length is sufficiently large relative to the grain diameter l ($l \ll \sqrt{D_{\text{eff}}^* t}$), D_{eff}^* can be expressed as⁴⁴

$$\frac{l + \delta}{D_{\text{eff}}^*} = \frac{l}{D_{\text{bulk}}^*} + \frac{\delta}{D_{\text{gb}}^*}, \quad (5)$$

where δ is the thickness of the grain boundary. This equation also represents the 1D case of the Maxwell–Garnett equation for calculating the diffusion coefficient in a two-phase material.^{38,39} As l is much larger than δ ($l \gg \delta$), D_{eff}^* is given by

$$D_{\text{eff}}^* = \frac{1}{(D_{\text{bulk}}^*)^{-1} + \left(\frac{l}{\delta} D_{\text{gb}}^*\right)^{-1}}. \quad (6)$$

We use $D_{\text{gb}}^*/\delta = 2.8 \times 10^{-6} \text{ cm s}^{-1}$, as determined by SIMS imaging, and we again assume that D_{bulk}^* is equal to $D_{\text{NMR,bulk}} = 2.8 \times 10^{-8} \text{ cm}^2 \text{ s}^{-1}$.³³ The average particle size $l = 16 \pm 11 \mu\text{m}$ is determined *via* electron backscatter diffraction,³³ and the

results are shown in Supplementary Fig. S1 in the ESI.[†] When these values are substituted into eqn (6), the effective diffusion coefficient of the 1D model may be calculated as $D_{\text{eff}}^* = 2.3 \pm 1.4 \times 10^{-9} \text{ cm}^2 \text{ s}^{-1}$. This value is consistent with $D_{\text{eff}}^* = 3.0 \times 10^{-9} \text{ cm}^2 \text{ s}^{-1}$ for long-range diffusion determined experimentally based on the time evolution of the SIMS line analysis, as compared in the Arrhenius plot in Fig. 5b. Although it is a coarse approximation, the 1D series model explains the long-range Li diffusion in LLTO polycrystals very well. Extrapolating the Arrhenius plot, the D_{eff}^* value at -110°C is calculated to be $1 \times 10^{-14} \text{ cm}^2 \text{ s}^{-1}$. Assuming the time of the SIMS imaging to be $t = 5 \text{ h}$, the diffusion length $\sqrt{2D_{\text{eff}}^* t}$ is $0.2 \mu\text{m}$, which is smaller than the spatial resolution of SIMS imaging. The Li diffusion during the measurement is negligible. We confirm that -110°C is a suitable temperature for SIMS imaging measurements.

Fig. 5b also demonstrates the temperature dependence of $D_{\text{NMR,bulk}}^{33}$ and the conductivity diffusion coefficients of the bulk and total ($D_{\sigma,\text{bulk}}$ and $D_{\sigma,\text{total}}$) obtained using IS.³³ Here, $D_{\sigma,\text{bulk}}$ and $D_{\sigma,\text{total}}$ are calculated based on the Nernst–Einstein equation using the bulk and total ionic conductivities, respectively, and the number density of Li ($5.0 \times 10^{-21} \text{ cm}^{-3}$) in LLTO.^{45–47} The details of IS are provided in the ESI.[†] As we reported previously, $D_{\text{NMR,bulk}}$ is consistent with $D_{\sigma,\text{bulk}}$ over the entire temperature range, and both display non-Arrhenius behaviors at $>177^\circ\text{C}$.³³ On the other hand, D_{eff}^* represents the long-range diffusion including grain boundaries in LLTO, and thus it is comparable to $D_{\sigma,\text{total}}$; however, Fig. 5b shows slightly smaller values of D_{eff}^* than those of $D_{\sigma,\text{total}}$. In order to clarify the temperature dependence of D_{eff}^* and $D_{\sigma,\text{total}}$, let us separate the bulk and grain boundary contributions according to eqn (6).

Fig. 5c compares the Arrhenius plot of $(l/\delta)D_{\text{gb}}^*$, as calculated using eqn (6), assuming that $D_{\text{bulk}}^* = D_{\text{NMR,bulk}}$, with $(l/\delta)D_{\sigma,\text{gb}}$ calculated from the grain boundary conductivity obtained *via* IS.⁴⁸ The activation energies of $(l/\delta)D_{\text{gb}}^*$ and $(l/\delta)D_{\sigma,\text{gb}}$ show almost the same value of 0.43 eV . Molecular dynamics (MD) simulations have been used to calculate the activation energies of grain boundary diffusion in $\text{Li}_{0.16}\text{La}_{0.62}\text{TiO}_3$.⁴⁹ The activation energy of the $\Sigma 5$ grain boundary is predicted to be 0.36 eV , whereas that of D_{gb}^* in the experiment is 0.43 eV . The larger activation energy can be attributed to the random nature of the grain boundaries, with a low experimental consistency (Supplementary Fig. S1†). The relationship between the D_{gb}^* value and the type of grain boundary has been investigated only for small Σ values. Sasano *et al.* reported that the ionic conductivity does not decrease at special grain boundaries, such as $\Sigma 2$ grain boundaries in LLTO thin films and $\Sigma 5$ grain boundaries in polycrystalline LLTO.^{52,53} MD calculations also suggest a relationship between the type of grain boundary and the diffusion coefficients.⁴⁹ The polycrystalline LLTO used in this study consists mostly of random grain boundaries (Fig. S1†). Therefore, most grain boundaries had low D_{gb}^* values. A more detailed analysis will be performed in future studies.

The respective pre-exponential factors of $(l/\delta)D_{\text{gb}}^*$ and $(l/\delta)D_{\sigma,\text{gb}}$ are 0.048 and $0.20 \text{ cm}^2 \text{ s}^{-1}$. The Haven ratio ($H_R \equiv D^*/D_{\sigma,\text{gb}}$)

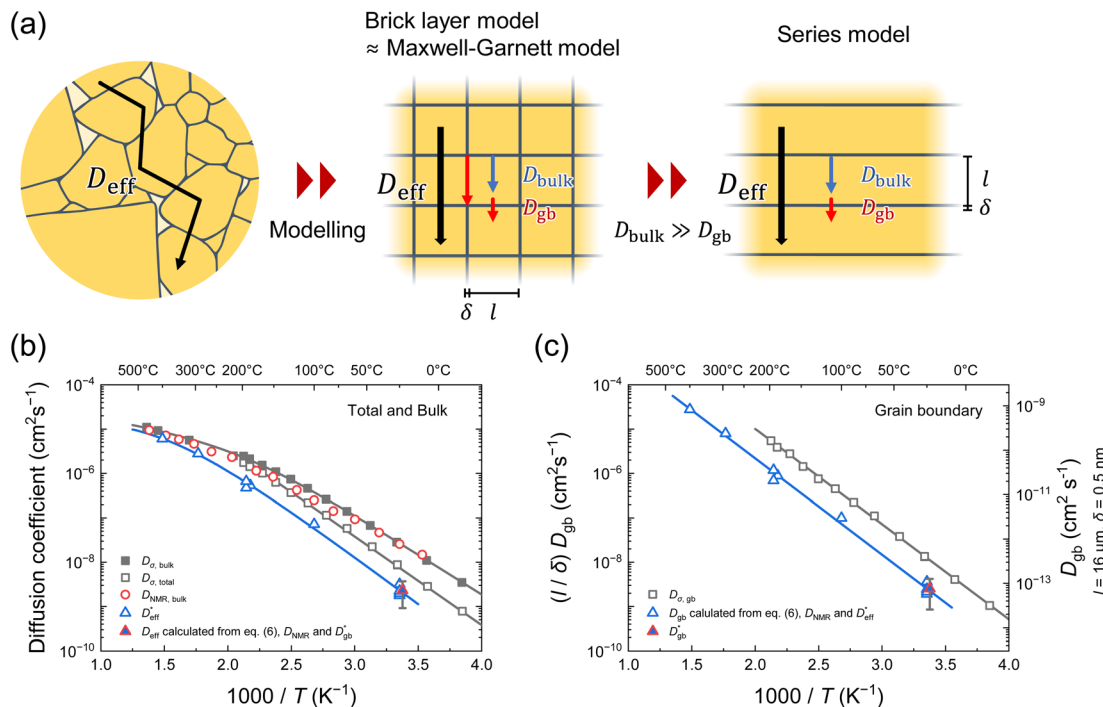


Fig. 5 (a) Ion diffusion modeling in polycrystals. The brick layer³⁹ and Maxwell–Garnett models³⁸ are generally used to model ion diffusion in polycrystalline materials. These models include two types of diffusion pathways: along and across the grain boundaries. When $D_{\text{bulk}} \gg D_{\text{gb}}$, diffusion along the grain boundaries may be ignored. Therefore, the series model of bulk and grain boundaries provides a good approximation. (b) Temperature dependences of the diffusion coefficients determined using the bulk³³ ($D_{\sigma,\text{bulk}}$, filled squares) and total conductivities ($D_{\sigma,\text{total}}$, open squares), PFG-NMR³³ ($D_{\text{NMR,bulk}}$, open circles), and SIMS line analysis (D_{eff} , open triangles). The D_{eff}^* calculated using the 1D model is also shown as a filled triangle. (c) Temperature dependences of $(l/\delta)D_{\text{gb}}$, as calculated using the grain boundary conductivity (open squares) and $(l/\delta)D_{\text{gb}}$, as determined via SIMS line and mapping analyses (open and filled triangles, respectively).

determined using the ratio of the pre-exponential factors is 0.24, which is smaller than the bulk ($H_{\text{R}} \approx 1$). Hence, we find that the separation of D_{eff}^* and $D_{\sigma,\text{total}}$ at low temperatures is due to the smaller H_{R} in the grain boundaries. There are two possible reasons for the smaller H_{R} of D_{gb} compared to that of D_{bulk} : the number of carriers at the grain boundary or the correlation effect is large.^{50,51} The grain boundaries of LLTO using transmission electron microscopy and Li depletion at the grain boundary were reported based on electron energy-loss spectra.^{36,52} Therefore, the possibility of increased carrier concentration should be eliminated, and thus, the correlation between the Li^+ ions is significant at the grain boundaries. Understanding the correlation effect will be the key to future breakthroughs in reducing grain boundary resistance.

Conclusions

We visualized and quantified the bulk and grain boundary diffusion of Li^+ ions in LLTO solid electrolytes using cryo-SIMS. The visualized image has revealed that the grain boundary impedes the ionic diffusion because of the much lower D_{gb}^* relative to D_{bulk}^* . The grain boundary diffusion coefficient, D_{gb}^* , has been determined to be $1.4 \times 10^{-13} \text{ cm}^2 \text{ s}^{-1}$ at 22 °C. The effective diffusion coefficient D_{eff}^* is explainable by D_{gb}^* and D_{bulk}^* by using a simple 1D model of bulk and grain boundaries. The activation energy of D_{gb}^* of 0.43 eV was consistent with the grain

boundary conductivity. H_{R} was small at the grain boundaries, suggesting enhanced correlation between the Li^+ ions at the grain boundaries. The SIMS method developed in this study effectively elucidates the bottleneck of ion transfer at the solid–solid interface, which limits the performance of charge/discharge rates and may contribute to improving the performance of solid-state lithium batteries.

Author contributions

G. H. and N. K. conceived the work. G. H. prepared and analyzed the samples. T. O. and K. T. helped with experimental design and interpretation of data. G. H. drafted the original manuscript. N. K., T. O. and K. T. revised the manuscript drafts.

Conflicts of interest

There are no conflicts to declare.

Acknowledgements

This study was supported by the Japan Science and Technology Agency ALCA-Specially Promoted Research for Innovative Next Generation Batteries project (grant number JPMJAL1301). This study was also supported by the Japan Society for the Promotion



of Science KAKENHI Grant Numbers JP19H05814 (Grant-in-Aid for Scientific Research on Innovative Areas “Interface IONICS”) and JP21H02033 (Grant-in-Aid for Scientific Research (B)). We thank Dr Atsuko Nagataki, Mr Kyosuke Matsushita, and Ms. Makiko Oshida for their assistance with SIMS and SEM at the NIMS Battery Research Platform (Tsukuba, Japan).

References

- 1 T. Famprakis, P. Canepa, J. A. Dawson, M. S. Islam and C. Masquelier, *Nat. Mater.*, 2019, **18**, 1278–1291.
- 2 K. Takada, *J. Power Sources*, 2018, **394**, 74–85.
- 3 L. Xu, S. Tang, Y. Cheng, K. Wang, J. Liang, C. Liu, Y.-C. Cao, F. Wei and L. Mai, *Joule*, 2018, **2**, 1991–2015.
- 4 M. Pasta, D. Armstrong, Z. L. Brown, J. Bu, M. R. Castell, P. Chen, A. Cocks, S. A. Corr, E. J. Cussen, E. Darnbrough, V. Deshpande, C. Doerrer, M. S. Dyer, H. El-Shinawi, N. Fleck, P. Grant, G. L. Gregory, C. Grovenor, L. J. Hardwick, J. T. S. Irvine, H. J. Lee, G. Li, E. Liberti, I. McClelland, C. Monroe, P. D. Nellist, P. R. Shearing, E. Shoko, W. Song, D. S. Jolly, C. I. Thomas, S. J. Turrell, M. Vestli, C. K. Williams, Y. Zhou and P. G. Bruce, *J. Phys. Energy*, 2020, **2**, 32008.
- 5 N. Ohta, K. Takada, L. Zhang, R. Ma, M. Osada and T. Sasaki, *Adv. Mater.*, 2006, **18**, 2226–2229.
- 6 A. L. Robinson and J. Janek, *MRS Bull.*, 2014, **39**, 1046–1047.
- 7 Y. Morino, H. Sano, T. Takahashi, N. Miyashita, A. Sakuda and A. Hayashi, *J. Phys. Chem. C*, 2023, **127**, 13616–13622.
- 8 J. F. Wu and X. Guo, *Phys. Chem. Chem. Phys.*, 2017, **19**, 5880–5887.
- 9 Y. Nomura, K. Yamamoto, Y. Yamagishi and E. Igaki, *ACS Nano*, 2021, **15**, 19806–19814.
- 10 Y. Kimura, A. Tomura, M. Fakkao, T. Nakamura, N. Ishiguro, O. Sekizawa, K. Nitta, T. Uruga, T. Okumura, M. Tada, Y. Uchimoto and K. Amezawa, *J. Phys. Chem. Lett.*, 2020, **11**, 3629–3636.
- 11 N. Schön, D. C. Gunduz, S. Yu, H. Tempel, R. Schierholz and F. Hausen, *Beilstein J. Nanotechnol.*, 2018, **9**, 1564–1572.
- 12 B. Steele, J. Kilner, P. Dennis, A. McHale, M. Van Hemert and A. Buggraaf, *Solid State Ionics*, 1986, **18–19**, 1038–1044.
- 13 M. Sase, K. Yashiro, K. Sato, J. Mizusaki, T. Kawada, N. Sakai, K. Yamaji, T. Horita and H. Yokokawa, *Solid State Ionics*, 2008, **178**, 1843–1852.
- 14 D. Uxa, H. J. Holmes, K. Meyer, L. Dörrer and H. Schmidt, *Phys. Chem. Chem. Phys.*, 2021, **23**, 5992–5998.
- 15 G. Hasegawa, N. Kuwata, Y. Tanaka, T. Miyazaki, N. Ishigaki, K. Takada and J. Kawamura, *Phys. Chem. Chem. Phys.*, 2021, **23**, 2438–2448.
- 16 K. Watanabe, I. Sakaguchi, S. Hishita, N. Ohashi and H. Haneda, *Appl. Phys. Express*, 2011, **4**, 055801.
- 17 J. Rahn, E. Hüger, L. Dörrer, B. Ruprecht, P. Heijmans and H. Schmidt, *Z. Phys. Chem.*, 2012, **226**, 439–448.
- 18 N. Kuwata, X. Lu, T. Miyazaki, Y. Iwai, T. Tanabe and J. Kawamura, *Solid State Ionics*, 2016, **294**, 59–66.
- 19 E. Navickas, Y. Chen, Q. Lu, W. Wallisch, T. M. Huber, J. Bernardi, M. Stöger-Pollach, G. Friedbacher, H. Hutter, B. Yıldız and J. Fleig, *ACS Nano*, 2017, **11**, 11475–11487.
- 20 N. Kuwata, M. Nakane, T. Miyazaki, K. Mitsuishi and J. Kawamura, *Solid State Ionics*, 2018, **320**, 266–271.
- 21 C. Schwab, A. Höweling, A. Windmüller, J. Gonzalez-Julian, S. Möller, J. R. Binder, S. Uhlenbrück, O. Guillon and M. Martin, *Phys. Chem. Chem. Phys.*, 2019, **21**, 26066–26076.
- 22 N. Kuwata, G. Hasegawa, D. Maeda, N. Ishigaki, T. Miyazaki and J. Kawamura, *J. Phys. Chem. C*, 2020, **124**, 22981–22992.
- 23 R. H. Brugge, R. J. Chater, J. A. Kilner and A. Aguadero, *J. Phys. Energy*, 2021, **3**, 034001.
- 24 H. Téllez, A. Aguadero, J. Druce, M. Burriel, S. Fearn, T. Ishihara, D. S. McPhail and J. A. Kilner, *J. Anal. At. Spectrom.*, 2014, **29**, 1361–1370.
- 25 R. Metzner, M. R. Thorpe, U. Breuer, P. Blümller, U. Schurr, H. U. Schneider and W. H. Schroeder, *Plant. Cell Environ.*, 2010, **33**, 1393–1407.
- 26 J. Zhang, J. Brown, D. J. Scurr, A. Bullen, K. MacLellan-Gibson, P. Williams, M. R. Alexander, K. R. Hardie, I. S. Gilmore and P. D. Rakowska, *Anal. Chem.*, 2020, **92**, 9008–9015.
- 27 Y. Inaguma, C. Liquan, M. Itoh, T. Nakamura, T. Uchida, H. Ikuta and M. Wakihara, *Solid State Commun.*, 1993, **86**, 689–693.
- 28 S. Stramare, V. Thangadurai and W. Weppner, *Chem. Mater.*, 2003, **15**, 3974–3990.
- 29 M. J. Wang, J. B. Wolfenstein and J. Sakamoto, *Adv. Funct. Mater.*, 2020, **30**, 1909140.
- 30 L. Zhang, X. Zhang, G. Tian, Q. Zhang, M. Knapp, H. Ehrenberg, G. Chen, Z. Shen, G. Yang, L. Gu and F. Du, *Nat. Commun.*, 2020, **11**, 3490.
- 31 Y. Mishin and C. Herzig, *Mater. Sci. Eng. A*, 1999, **260**, 55–71.
- 32 P. Heijmans and S. Indris, *J. Phys.: Condens. Matter*, 2003, **15**, R1257–R1289.
- 33 G. Hasegawa, N. Kuwata, K. Hashi, Y. Tanaka and K. Takada, *Chem. Mater.*, 2023, **35**, 3815–3824.
- 34 Y. Inaguma, *J. Ceram. Soc. Jpn.*, 2006, **114**, 1103–1110.
- 35 X. Gao, C. A. J. Fisher, T. Kimura, Y. H. Ikuhara, A. Kuwabara, H. Moriwake, H. Oki, T. Tojigamori, K. Kohama and Y. Ikuhara, *J. Mater. Chem. A*, 2014, **2**, 843–852.
- 36 C. Ma, K. Chen, C. Liang, C.-W. Nan, R. Ishikawa, K. More and M. Chi, *Energy Environ. Sci.*, 2014, **7**, 1638–1642.
- 37 H. Mehrer, *Diffusion in Solids: Fundamentals, Methods, Materials, Diffusion-Controlled Processes*, Springer Science & Business Media, 2007, ch. 32.
- 38 J. R. Kalnin, E. A. Kotomin and J. Maier, *J. Phys. Chem. Solids*, 2002, **63**, 449–456.
- 39 I. V. Belova and G. E. Murch, *J. Phys. Chem. Solids*, 2003, **64**, 873–878.
- 40 H. Mehrer, *Diffusion in Solids: Fundamentals, Methods, Materials, Diffusion-Controlled Processes*, Springer Science & Business Media, 2007, ch. 34.
- 41 J. Crank, *The Mathematics of Diffusion*, Clarendon Press, 1975, ch. 3.
- 42 H. Mehrer, *Diffusion in Solids: Fundamentals, Methods, Materials, Diffusion-Controlled Processes*, Springer Science & Business Media, 2007, ch. 3.
- 43 J. C. Fisher, *J. Appl. Phys.*, 1951, **22**, 74–77.



44 J. Crank, *The Mathematics of Diffusion*, Clarendon Press, 1975, ch. 12.

45 T. Zinkevich, B. Schwarz, P. Braun, A. Weber, H. Ehrenberg and S. Indris, *Solid State Ionics*, 2020, **357**, 115486.

46 Y. Q. Cheng, Z. H. Bi, A. Huq, M. Feygenson, C. A. Bridges, M. P. Paranthaman and B. G. Sumpter, *J. Mater. Chem. A*, 2014, **2**, 2418–2426.

47 A. Varez, M. T. Fernández-Díaz, J. A. Alonso and J. Sanz, *Chem. Mater.*, 2005, **17**, 2404–2412.

48 T. van Dijk and A. J. Burggraaf, *Phys. Status Solidi*, 1981, **63**, 229–240.

49 A. R. Symington, M. Molinari, J. A. Dawson, J. M. Statham, J. Purton, P. Canepa and S. C. Parker, *J. Mater. Chem. A*, 2021, **9**, 6487–6498.

50 G. E. Murch, *Solid State Ionics*, 1982, **7**, 177–198.

51 A. Van der Ven, Z. Deng, S. Banerjee and S. P. Ong, *Chem. Rev.*, 2020, **120**, 6977–7019.

52 S. Sasano, R. Ishikawa, G. Sánchez-Santolino, H. Ohta, N. Shibata and Y. Ikuhara, *Nano Lett.*, 2021, **21**, 6282–6288.

53 S. Sasano, R. Ishikawa, K. Kawahara, T. Kimura, Y. H. Ikuhara, N. Shibata and Y. Ikuhara, *Appl. Phys. Lett.*, 2020, **116**, 043901.

